MEDICAL ROBOTS

Catalytic antimicrobial robots for biofilm eradication

Geelsu Hwang[1]*, Amauri J. Paula[1,2]*, Elizabeth E. Hunter[3], Yuan Liu[1], Alaa Babeer[1,4], Bekir Karabucak[4], Kathleen Stebe[5], Vijay Kumar[3], Edward Steager[3]†, Hyun Koo[1]†

Magnetically driven robots can perform complex functions in biological settings with minimal destruction. However, robots designed to damage deleterious biostructures may also be useful. Biofilms are intractable, firmly attached structures associated with drug-resistant infections and surface destruction. We designed catalytic antimicrobial robots (CARs) that precisely, efficiently, and controllably killed, degraded, and removed biofilms. CARs exploiting iron oxide nanoparticles (NPs) with dual catalytic-magnetic functionality (i) generated bactericidal free radicals, (ii) broke down the biofilm exopolysaccharide (EPS) matrix, and (iii) removed the fragmented biofilm debris via magnetic field–driven robotic assemblies. We developed two distinct CAR platforms. The biohybrid CAR platform was formed from NPs and biofilm degradation products. After catalytic bacterial killing and EPS disruption, magnetic field gradients assembled NPs and the biodegraded products into a plow-like superstructure. When driven with an external magnetic field, the biohybrid CAR completely removed biomass in a controlled manner, preventing biofilm regrowth. Biohybrid CARs could be swept over broad swathes of surface or moved over well-defined paths for localized removal with microscale precision. The 3D molded CAR platform is a polymeric soft robot with embedded catalytic-magnetic NPs, formed in a customized 3D-printed mold to perform specific tasks in enclosed domains. Vane-shaped CARs remove biofilms from curved walls of cylindrical tubes, and helicoid-shaped CARs drill through biofilm clogs while simultaneously killing bacteria. We demonstrate applications of CARs to target highly confined anatomical surfaces in the interior of human teeth. These "kill-degrade-and-remove" CARs systems may fight persistent biofilm infections and mitigate biofouling of medical devices and diverse surfaces.

INTRODUCTION

Biofilms, surface-associated bacterial communities, are notoriously difficult to treat and remove (*1*, *2*). They form on abiotic surfaces (implants and catheters) and biotic surfaces (teeth and mucosal), often in difficult-to-access spaces, with deleterious effects that include persistent infections and medical complications (*3*, *4*). In addition, biofilms clog water lines, pipes, and crevices in industrial settings (*2*, *4*). Biofilms contain bacterial cells surrounded by a matrix of extracellular polymeric materials, such as exopolysaccharides (EPS), which provide adhesion and cohesion to the biofilm structure (*2*). These complex and mechanically stable scaffolds also act as barriers to antibacterial drugs, protecting bacteria within them (*1*, *4*). The effective eradication of biofilms poses a substantial technical and societal challenge especially as we approach a post-antibiotic era. Current antimicrobial approaches are largely ineffective because they fail to address simultaneously biofilm structural and biological properties associated with drug resistance (*3*) and biofilms' ability to rapidly re-establish themselves if matrix debris and bacteria are not removed. Thus, new technologies are needed to effectively target the biofilm structure, kill the bacterial cells embedded within, and remove the degraded products. Such a "kill-degrade-and-remove" biofilm disruption approach may be achieved using robotics.

Robots, dynamic systems with controlled movement and force generation, have been explored in diverse applications ranging from drug delivery to precision therapeutics (*5*, *6*). Magnetic robotic actuation is attractive because it allows tether-free controlled motion and enables a wide variety of robotic motility and locomotion strategies (*7*, *8*). Under suitable conditions, magnetic fields easily and harmlessly penetrate most biological and synthetic materials and can direct particle motion in confined spaces (*5*, *8*). Although robots have been developed for specific tasks such as targeted cargo delivery, manipulation of particles and cells, and multimodal locomotion (*8*, *9*), applications for physical and chemical biofilm disruption have yet to be developed.

Here, we developed catalytic antimicrobial robots (CARs) capable of performing multiple tasks for effective biofilm elimination by simultaneously targeting drug and mechanical resistance factors (Fig. 1A). The CARs' catalytic activity chemically killed bacteria and degraded the biofilm matrix, and their magnetic actuation physically removed the biofilm from surfaces. These magneto-catalytic capabilities rely on iron oxide nanoparticles (NPs) (Fig. 1B) with intrinsic enzyme-like (i.e., peroxidase) properties (*10*). These NPs catalyze hydrogen peroxide to generate reactive antibiofilm molecules (*11*, *12*). Furthermore, iron oxide NPs in suspension or encapsulated in other structures can be directed to biofilm locations using magnetic fields (*13*, *14*). With these principles, we present two small-scale robotic platforms that incorporate iron oxide NPs (Fig. 1C) to kill and clean biofilms on surfaces or in difficult-to-access, confined spaces. Robots drive along specific paths to precisely and controllably tear down and scrub away dead bacteria and biofilm debris. The ability to dictate the location of bactericidal action allows targeted biofilm disruption on surfaces or in inaccessible locations, and debris removal is central to the prevention of biofilm regrowth. The incorporation of the catalytic killing-degrading modality that acts in concert with magnetic properties introduces a conceptual framework for a robotics platform to achieve unprecedented ability to eradicate biofilms.

---

[1]Biofilm Research Labs, Levy Center for Oral Health, Department of Orthodontics, School of Dental Medicine, University of Pennsylvania, Philadelphia, PA, USA. [2]Solid-Biological Interface Group (SolBIN), Department of Physics, Universidade Federal do Ceará, Fortaleza, CE, Brazil. [3]GRASP Laboratory, School of Engineering and Applied Science, University of Pennsylvania, Philadelphia, PA, USA. [4]Department of Endodontics, School of Dental Medicine, University of Pennsylvania, Philadelphia, PA, USA. [5]Department of Chemical and Biomolecular Engineering, University of Pennsylvania, Philadelphia, PA, USA.
*These authors contributed equally to this work.
†Corresponding author. Email: esteager@seas.upenn.edu (E.S.); koohy@upenn.edu (H.K.)

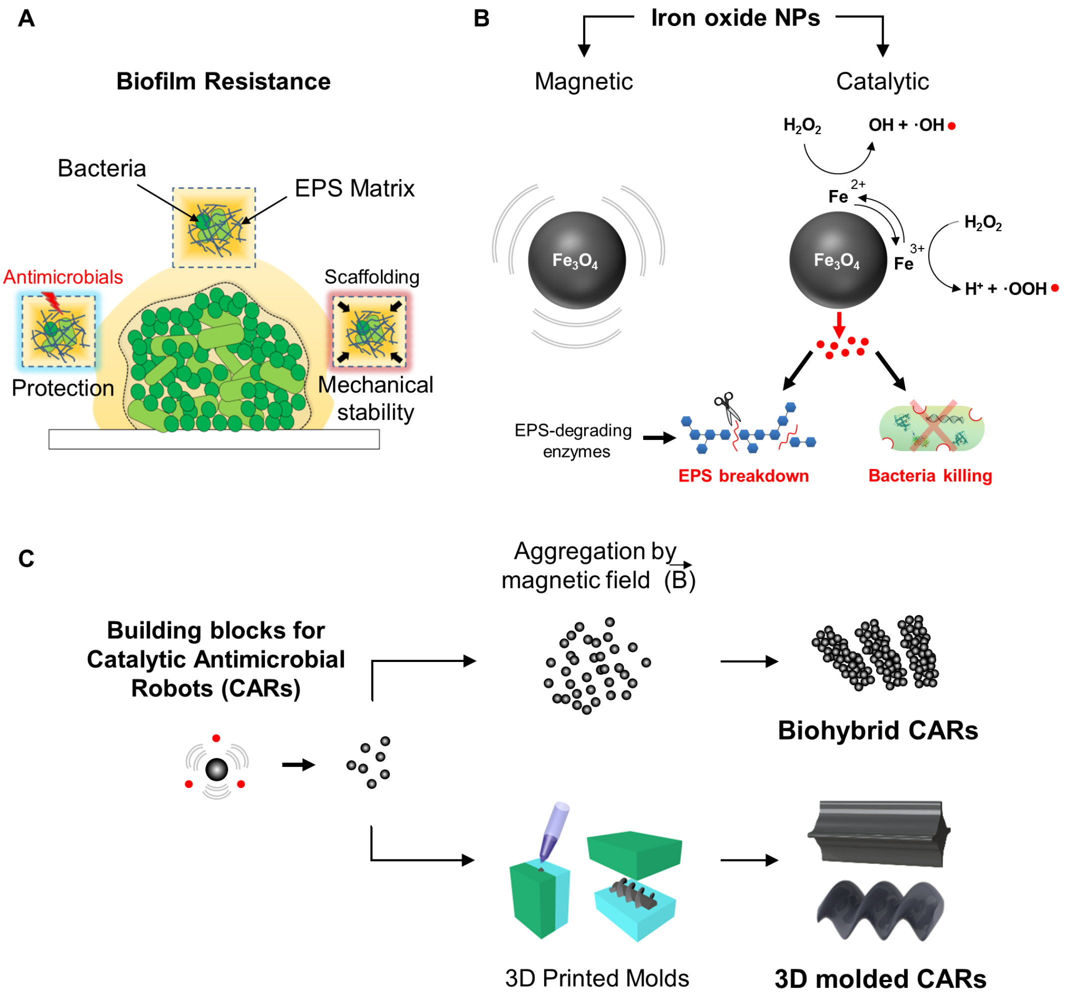

Fig. 1. Catalytic and magnetic iron oxide NPs as building blocks for small-scale robots designed for biofilm killing and removal. (**A**) Diagram illustrating the challenges of biofilm removal due to the EPS matrix that provides protection against antimicrobials and mechanical stability (*3*, *4*). (**B**) Diagram depicting the magnetic-catalytic NPs and their bacterial killing and EPS degradation mechanisms via reactive free radicals generated from hydrogen peroxide (H_2O_2) via peroxidase-like activity. The EPS degrading activity was enhanced by addition of mutanase/dextranase to digest extracellular glucans. (**C**) Catalytic-magnetic NPs in suspension served as multifunctional building blocks to form CARs. In the first CAR platform, biohybrid CARs with bristle-like structures were assembled from NPs suspended in H_2O_2 and mutanase/dextranase solution by a permanent magnet attached to a micromanipulator and used to remove biofilms from accessible surfaces. In a second platform, catalytic-magnetic NPs were embedded into gels to form 3D molded CARs having specialized vane and helicoid structures.

RESULTS

Characterization and optimization of magneto-catalytic NPs

We developed robotic biofilm killing and removal platforms that exploit catalytic-magnetic NPs in a formulation designed to enhance their catalytic activity. Iron oxide NPs (213 ± 26.5 nm in diameter) catalyze hydrogen peroxide (H_2O_2) to generate free radicals that potently kill biofilm-embedded bacteria (*10*–*12*). These free radicals can also degrade the biofilm EPS matrix, albeit more slowly than their bactericidal action (*15*). The EPS degradation rate can be enhanced with EPS-degrading enzymes mutanase/dextranase that assist the breakdown of (α-1,3)– and (α-1,6)–linked extracellular glucans in the biofilm (*16*). We thus formulated NP suspensions (2000 μg ml^{-1}) with 1% H_2O_2 and 1.75/8.75 U mutanase/dextranase for maximal efficacy of bacterial killing and EPS degradation (fig. S1). Confocal imaging reveals that entire clusters of bacteria were killed, and the EPS matrix was effectively dismantled after exposing the biofilm to the NP catalytic formulation (fig. S1). However, if not removed, biofilm debris serves as a reservoir of nutrients and facilitates attachment and growth of bacterial cells, reinitiating the biofilm life cycle (*2*, *3*). Thus, removal of the cellular and matrix debris is of paramount importance to persistent eradication of biofilms. This can be achieved by leveraging the magnetic properties of NPs to create CARs.

To characterize the magnetic force on the dispersed NPs, we studied their motion in a viscous medium (Fig. 2A). A cylindrically shaped permanent magnet with a diameter of 2 mm was placed beneath the NP suspension (200 μg NP in 100 μl of 50% glycerol), and the particle accumulation was recorded. The gray scale of the suspension (Fig. 2, B and C) serves as a proxy for the particle concentration, where $x = 0$ is the center of the magnet (details in fig. S2). The NPs accumulated above the magnet with pronounced peaks near the magnet's sharp edges, where the field gradients were highest. A balance of viscous and magnetic forces allowed the magnetic force on a 2-μm-diameter aggregate of NPs to be estimated to be ~30 pN (details in Materials and Methods). The particles formed a cluster whose size depended on the concentration of NPs (Fig. 2D) and the movement of the permanent magnet defined by an automated displacement routine via a control algorithm for specific motion patterns (Fig. 2E). The control algorithms for this work were programmed using open-loop control, in which motion patterns were preprogrammed on the basis of modeling of system dynamics (details in Materials and Methods).

We then dispensed the same concentration of NP dispersion (2000 μg ml^{-1} NP) over the biofilm-covered surface and assessed the bioactivity and motion of the NPs without and with catalytic activation. Time-lapse imaging revealed that the NPs (absent catalysis) on the biofilm failed to aggregate in the presence of the magnetic field. These NPs did not move in response to the magnet (Fig. 3A, top panel) as observed in glycerol using the same magnet. Rather, upon contact with the biofilm, the NPs adhered and were unable to form a cluster (Fig. 3, A and B). Furthermore, NPs without catalytic activation neither killed bacteria nor degraded the EPS (Fig. 3C and fig. S1).

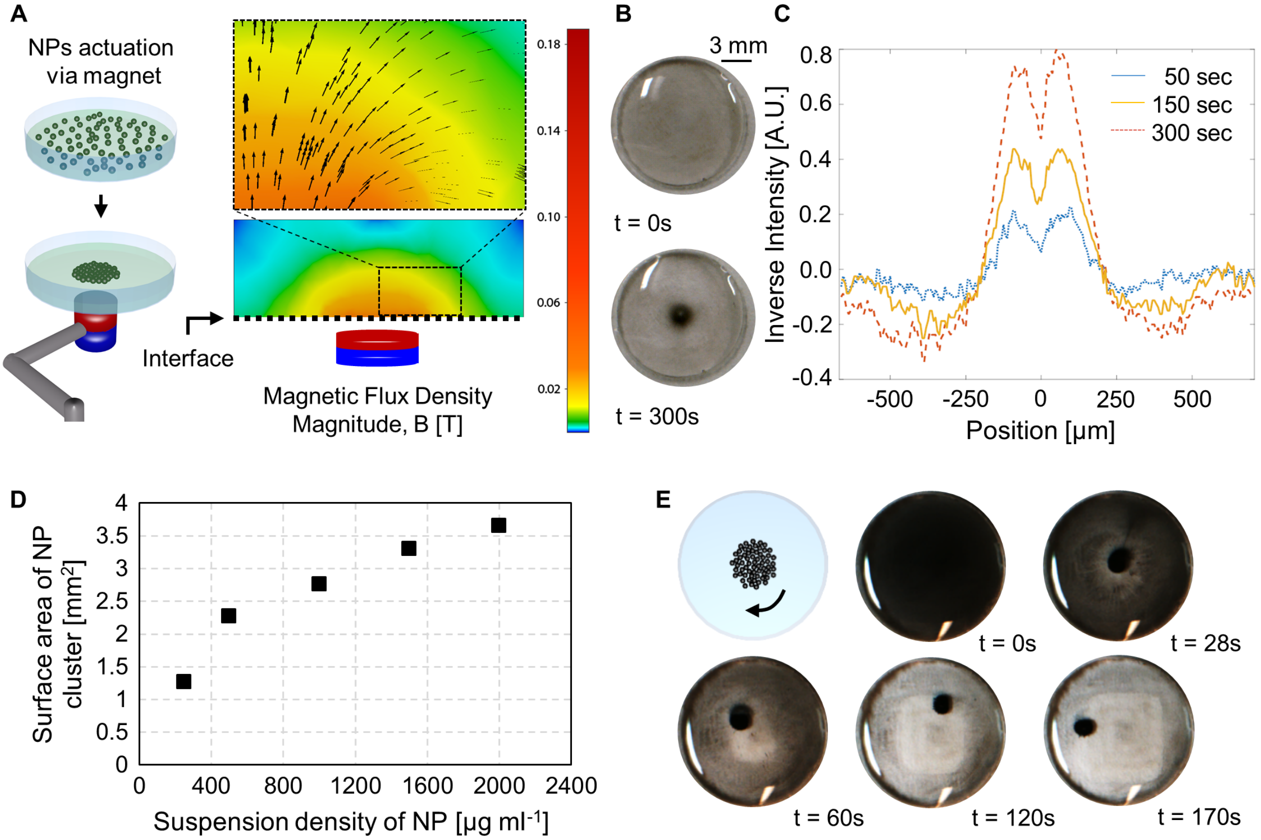

Fig. 2. Characterization of NPs in a model solution. (**A**) Cylindrical magnet placement using a micromanipulator and magnetic flux density. (**B**) NP cluster in suspension before and after magnetic actuation and (**C**) time-lapse quantification of NP cluster using MATLAB. (**D**) Surface area of the cluster versus suspension density of NP determined from still images 300 s after magnetic flux application using an optical thresholding method. (**E**) Motion of NP cluster under magnetic control. Initially, an NP cluster with a circular footprint was formed, centered above the magnet. Suspended NPs moved toward the NP cluster, which was moved in a preprogrammed trajectory, clearing the solution.

Upon catalytic activation, however, NPs not only killed the bacteria and degraded the EPS but also adhered to and interacted with the biofilm debris to form a cluster in the presence of the magnet [Fig. 3, A (bottom panel) and B, and fig. S1]. Quantitative analysis shows that the size of the cluster increased with time (Fig. 3B), indicating a critical role of both catalytic activity and magnetic actuation for NP aggregation. Furthermore, high-resolution confocal microscopy revealed that the NPs formed a superstructure in this setting whereby micrometer-scale, rod-like oriented NP aggregates were enmeshed with biofilm debris (Fig. 3D and fig. S3) to form a bio-inorganic hybrid assemblage.

Biofilm removal by biohybrid CARs

Motivated by these findings, we used the NP dispersions in a stepwise approach to kill, degrade, and remove biofilms (Fig. 4, A and B). NPs suspended in a solution of H_2O_2 and enzymes were placed onto the biofilm. After catalytic disruption of the biofilm was initiated, the NPs were pulled toward the degraded biofilm-covered surface using a permanent magnet. Orthogonal confocal imaging showed that these rod-like biohybrid aggregates assembled across the biofilm thickness to form vertically oriented bristles via magnetic field gradients (Fig. 4A). This cluster was then moved over the surface via a Siskiyou three-axis manipulator with 0.1-µm precision and point-to-point accuracy of 2 µm. During this process, the cluster morphed into a C-shaped aggregate (Fig. 4C) to plow through and remove the biofilm (Fig. 4D). Thus, the NPs became building blocks for robotic superstructures formed by directed assembly under the action of the magnetic field. The assembly formation relied on NP catalytic properties to break down the biofilm and kill the bacteria, their interactions with the biofilm debris to allow adhesion between these elements, and their magnetic properties to allow the superstructure to form in geometries influenced by the dynamics of the external field (Fig. 4, B and C). These biohybrid CARs constitute our first robotic platform.

Different biofilm cleaning modes could be selected by tuning the size of the biohybrid CARs. For example, a 150-mm^2 wafer covered with biofilm could be swept clean by forming a 3.5-mm^2 biohybrid CAR and driving it methodically over the substrate using a permanent magnet coupled to a micromanipulator (Fig. 4, A and B). Initially, 100-µl (200 µg of NPs) aliquot of dispersed NPs suspension was pipetted over the entire biofilm surface. After 30 min of catalysis-mediated biofilm disruption, the magnetic field was applied. The biohybrid CAR formed within a circular magnetic field established in the plane of the biofilm for 1 min. This field pulled the NPs through the biofilm to the biofilm-glass surface (fig. S4). Thereafter, the magnetic field was cycled to move the biohybrid CARs in a circular pattern across the surface. During this process, NPs were continually recruited from

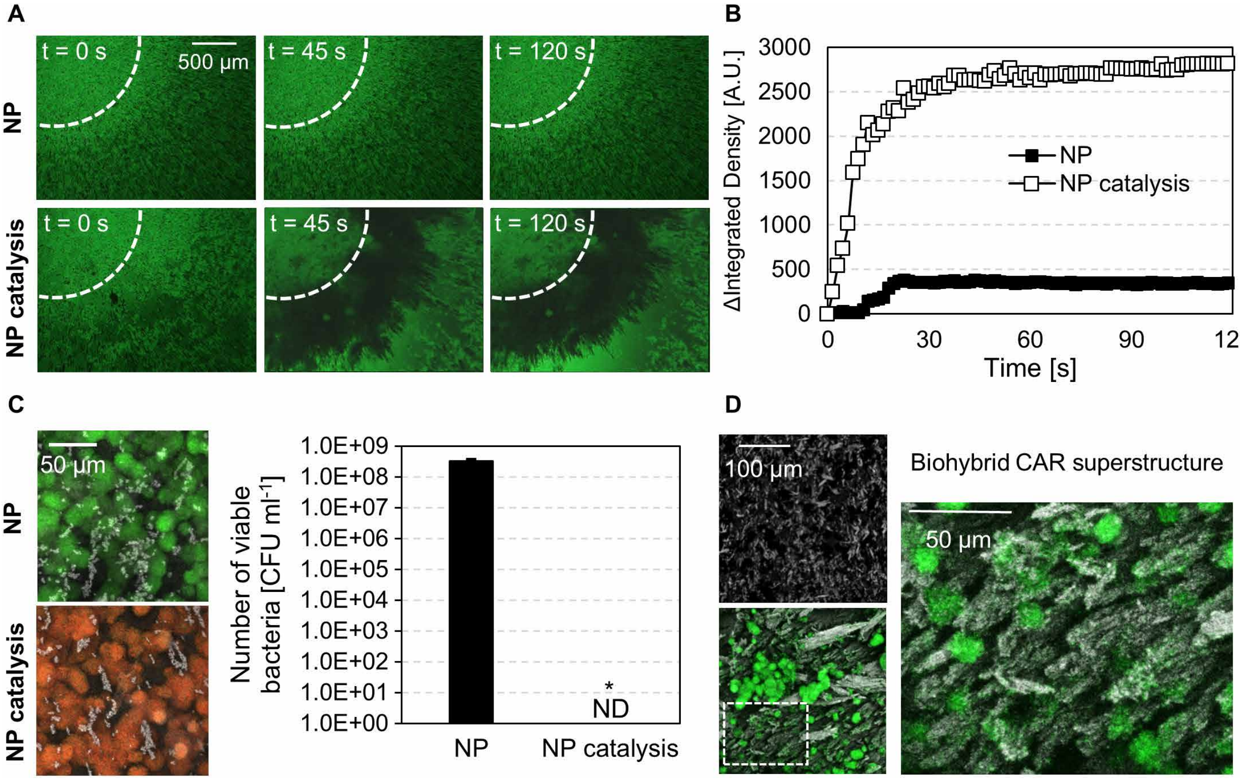

Fig. 3. Characterization and formation of biohybrid CARs. (**A**) NP actuation in biofilm in the presence of magnetic field. *S. mutans*, a biofilm-forming model organism and a bacterial oral pathogen, was used to form biofilms. NPs, absent catalysis, did not aggregate owing to adhesive interactions with the biofilm. Conversely, NPs with catalysis degraded the biofilm and moved toward the magnet to assemble into a cluster. (**B**) Quantitative imaging analysis shows the size of cluster in NP with and without catalysis [as shown in (A)]. (**C**) Data from bacterial viability assays using fluorescence imaging and culturing methods. Green fluorescence indicates live bacteria and red indicates dead bacteria, and the number of viable cells as determined by CFU counting. The data show that NPs alone were devoid of antibacterial activity, whereas NPs with catalysis potently killed bacteria. Error bars indicate standard deviation; ND, not detected. (**D**) Biohybrid CAR superstructure is revealed by high-resolution confocal microscopy. Absent catalytic activity, only small NPs assemblages formed (top panel). With catalytic activity, biohybrid CARs formed; they consisted of a complex bio-inorganic hybrid assemblage comprising spatially oriented, rod-like, micrometer-size superstructures of NP enmeshed with bacterial mass and debris (bottom and right panels).

the bulk, increasing the size/density of the biohybrid CARs as the experiment proceeded (fig. S4). By defining a trajectory that started at the center of the workspace and progressively swept outward in a concentric manner, the biohybrid CARs cleared the biofilm biomass away from the contaminated surface (Fig. Fig. 4, B and D). The absence of bacteria over the surface after the biohybrid CAR's displacement was confirmed with lack of fluorescent signal from SYTO 9–labeled bacteria (Fig. 4D, far right panel), indicating the ability of large-scale cleaning (at the centimeter scale). It is imperative that bacterial cells are killed, that the biofilm is degraded, and that biofilm debris is removed to avoid regrowth of biofilm (*1*, *3*, *4*). Thus, we assessed whether biofilms could regrow after treatment with CARs by incubating the cleared surface in growth culture medium for additional 24 hours (details in Materials and Methods). Neither viable bacterial cells nor biofilm regrowth was detected on surfaces treated with CARs (Fig. 4E and fig. S5), demonstrating efficacy of the robots for bacterial killing and biofilm degradation and removal.

Smaller biohybrid CARs can remove biofilms along preferred paths while leaving surrounding domains intact. This might be desirable, for example, to remove biofilms without damaging nearby host tissues or to sample biofilms at specific pathological sites, to identify microbial composition. By placing a droplet of the dispersed NP suspension near the location to be cleaned, the NP suspension can be concentrated near a focal point for highly localized biomass removal (Fig. 4F). To demonstrate this spatial targeting of specific biofilm sites, we moved 2-mm^2 biohybrid CARs to remove biofilms along predetermined trajectories to generate specific patterns, such as a circle, square, and triangle (Fig. 4G and movie S1). The biohybrid CARs cleared paths for complete removal of biofilm-covered areas with micrometer-scale geometrical precision with distinctive patterns (Fig. 4, F and G, and movie S1). High-magnification confocal images confirmed clearance of the cleaned area, delineated by sharp edges with distinct features such as curved contours, straight lines, and pointed patterns (Fig. 4G, far right panels). Thus, the biohybrid CARs could be steered to sweep surfaces effectively clean of biofilm debris for broad swathes or localized removal through synergistic combination of catalytic and magnetic properties. The relatively large NPs used in this study were targeted toward topical use or for use on or in contaminated structures with difficult access. Although these NPs have remanant magnetization, this property is not required for the biohybrid CARs. We have conducted additional experiments using Feraheme (ferumoxytol), a U.S. Food and Drug Administration (FDA)–approved formulation (*17*) composed of small dextran-coated iron oxide NPs (<20 nm) with negligible remanant magnetization (fig. S6). Catalytic activation and directed motion of CARs based on these smaller NPs using magnetic field gradients were sufficient to break

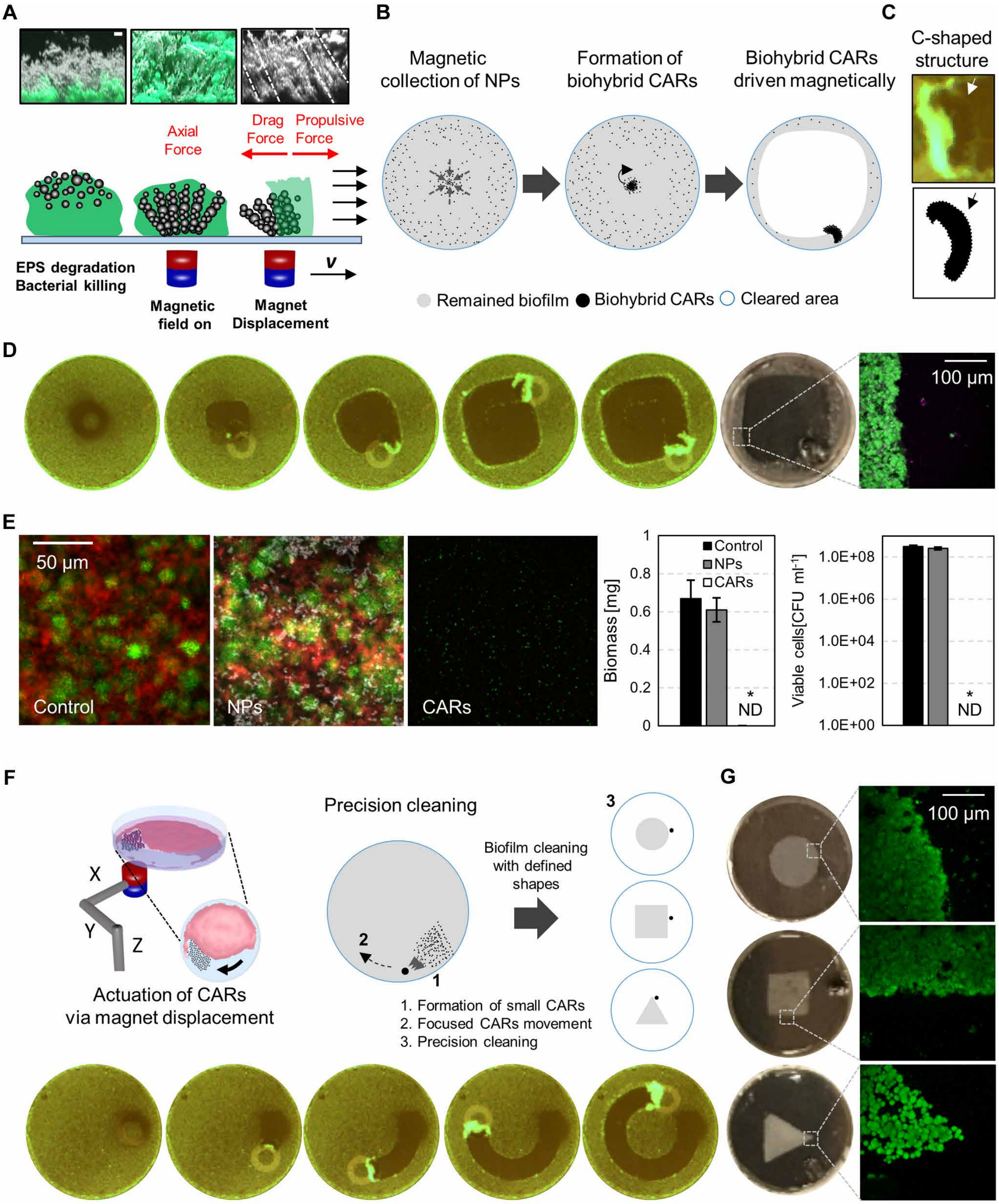

Fig. 4. Platform 1: Biofilm removal using biohybrid CARs. (**A**) Orthogonal view of biofilms treated with biohybrid CARs reveals the rod-like superstructure forming bristles (highlighted by white dashed lines) through the compromised biofilms. After incubation, biohybrid CARs were manipulated precisely using a magnetic field gradient to completely remove biofilms and biofilm debris, including dead bacteria and degraded EPS, from surfaces. Scale bar indicates 10 μm. (**B**) Diagram depicting cleaning of large areas of a biofilm-coated surface by magnetically controlled sweeping of biohybrid CARs (after bacterial killing/EPS degradation). (**C**) The biohybrid CAR morphed into C-shaped aggregate (see arrows) as it moved over the surface to plow through and remove biofilm (labeled with SYTO 9 green fluorescence). (**D**) Fluorescent images indicating complete cleaning of an *S. mutans* biofilm (labeled in green) grown on a glass surface by using biohybrid CARs sweeping effect. (**E**) Biofilm-removed surfaces were incubated for additional 24 hours with the biofilm growth medium (supplemented with 1% sucrose) to assess bacterial regrowth using confocal microscopy and culturing methods. There is no biofilm regrowth on biofilm-removed surfaces by CARs even after 24 hours incubation. Control and NP-treated biofilms were also incubated using the same conditions, both showing abundant bacterial cells (in green) and EPS (in red); quantitative analyses show high amounts of biomass and high number of viable cells. Quantitative data also confirm that there was no detectable biomass or viable cells with treatment by CARs. Error bars indicate standard deviation. (**F**) The controlled movement of focused biohybrid CARs resulted in precise removal of biofilms from surfaces with defined geometrical shapes. (**G**) Fluorescent microscopy confirms the complete removal of bacteria from the surface.

down and remove biofilms, although the mechanism of disruption and collection differed significantly from that with larger NPs, which yielded large aggregates and biohybrid superstructures. Nevertheless, the data collectively show that catalytic activity is the key for bacterial killing and biofilm degradation, and programmed displacement of the CARs allowed them to collect debris as they proceeded along given paths. Further, the CARs superstructure effectively removed biofilms, whereas the NPs without catalytic activation did not, indicating that magnetic properties alone were insufficient for complete biofilm removal.

Biofilm removal by small-scale 3D molded CARs

Biofilms do not only form on accessible surfaces in exposed areas. Rather, they often form in inaccessible locations featuring confining geometries (catheters and water lines) and are challenging to eradicate, creating clogs that cause infection or block fluid flow. To address this need, we embedded NPs in soft, water-based agar hydrogel to form magnetically driven three-dimensional (3D) molded CARs to perform specific tasks such as dislodging biofilms from the walls of cylindrical tubes or drilling biofilm clogs (Fig. 5). Printable and soft robotics enable the production of 3D structures with specific geometries with a single or few input commands (*18*, *19*). Here, we exploited a facile, single-step molding technique to fabricate customized 3D small-scale magnetic robots (*20*). This method allows incorporation of functional additives and materials without additional fabrication steps like those required in conventional 3D printing at concentrations that would interfere with processes that rely on ultraviolet-activated cross-linkers (*21*, *22*). We incorporated NPs at high concentration (10%, w/v) by filling millimeter-scale 3D-printed molds with a thermo-reversible gelifying agar polymer. We formed two shapes (Fig. 5A), including double-helicoid CARs (formed from two helices wrapped around a central axis) and vane-like CARs with fin-like structures around a central core. The first shape was inspired by the propulsion efficacy of helical propellers that can penetrate physical barriers (*9*), whereas the latter shape was motivated by the success of vane-shaped tools at disrupting biofilms (see Supplementary Materials) (*23*).

Magnetic field gradients can drive small-scale robots and control their locomotion (*24*). Furthermore, rotating magnetic fields generated by rotating permanent magnets or electromagnetic coils have been used to drive helical or screw-shaped small-scale robots through fluids (*25*, *26*). By applying a magnetic torque, helical robots can be driven through soft tissues, gels, and blood clots to eliminate harmful blockages or to access interior spaces (*27*, *28*). Here, we used uniform-rotating magnetic fields generated by two pairs of nested Helmholtz coils (*20*) configured so that magnetic field strength and rotational frequency were controlled independently (Fig. 5B). In all experiments, robots were operated at the center of the workspace where fields were approximately uniform and measured 3.4 mT. Robots executed preprogrammed trajectories within a glass tube with a length of 450 mm and a diameter of 7 mm; the robot's position and velocity were captured by a high-speed complementary metal-oxide semiconductor camera (see Materials and Methods).

Both robots were magnetized along their short axis (Fig. 5C); this process relies on the NP remanant magnetization and the associated magnetic dipoles to achieve controlled rotation. As the magnetic field rotated, the robots realigned with the magnetic field direction. The rotation of the vane CARs allowed them to generate localized fluid shear stress and to scrub the walls of the tube (Supplementary Materials). Their translation relied on a magnetic field gradient along the axis, established by placing a permanent magnet at the end of the tube. The tube was filled with H_2O_2/enzyme solution and incubated at room temperature for at least 5 min. Because the agar hydrogel used to form the 3D molded CARs was permeable to H_2O_2, the reagent and NP catalyst within the robot formed the bactericidal products (fig. S7). As the rotating vane CAR was pulled through the tube, it made direct physical contact with the biofilm and generated frictional and fluid shear stresses. The magnitude of the shear stress could be estimated on the basis of the gap thickness and rate of rotation and determined to be 0.062 Pa, in keeping with previous studies on removal of EPS-defective biofilms (Supplementary Materials). Previously, we demonstrated that intact biofilms were only fractionally removed with high shear stress (1.78 Pa), whereas EPS-defective biofilms (EPS-digested or impaired EPS production) could be almost completely removed even with significantly lower shear force (0.1 to 0.2 Pa) (*23*, *29*). Thus, disruption of EPS matrix was critical to efficiently dislodge biofilms. In this study, we showed that biofilms at the wall of glass tubing could be removed by the shear force (~0.06 Pa) generated by the vane robot when the catalytic activity was present, consistent with our previous findings. By combined catalytic action and mechanical displacement, the rotating vane CAR driven into the tube could efficiently scrape and displace the degraded biofilm from walls, which formed a pile of debris (Fig. 5E) that could be cleared by flushing the tubing with water (fig. S8).

The chiral geometry of the helicoid CAR enabled forward motion from the applied magnetic torque (*20*) with a velocity proportional to the magnitude of the field and the rotation frequency (fig. S9A) (*30*). The helicoid CAR was propelled in a corkscrew-like fashion at an average velocity of 5 mm s^{-1} in the H_2O_2/enzyme solution. This motion made the helicoid CAR (Fig. 5A) suitable for drilling through biofilm occlusions and clearing biofilm clogs (Fig. 5, F and G, and movie S2). To demonstrate this concept, we formed biofilms at the end of conical tubing to mimic clogging plaque. Upon application of the rotating magnetic field, the helicoid CAR approached the clog and drilled through it, leaving a pile of biomass debris behind similar to debris generated by drill bit action (Fig. 5G, fig. S9b, and movie S2). The amount of removed biomass debris was plotted against various frequencies in fig. S8C, showing incremental increase of biomass debris with frequency. In addition, we demonstrated the ability of the helicoid CAR to remove occlusions and restore paths in biofilm-clogged tubes (Fig. 5H).

To confirm that the biofilm eradication was due to the synergistic effects between the catalytic and magnetic properties of NPs, we have performed control experiments with the molded helicoid CAR without catalytic activation (fig. S10). Established biofilms present high physical resistance, making them difficult to mechanically disrupt without EPS degradation. Under identical conditions, the helicoid CAR without catalysis failed to remove the clog, although biofilm disruption was observed as the robot cut through parts of the biomass from drilling. However, the bacteria cells released from physical drilling and those within the remaining biofilm clog remained viable (fig. S10). In contrast, the CAR with catalytic activation completely removed the biofilm clog and killed all bacteria, further underscoring the need for the degradation reaction as well as the robotic motion. Mechanical disruption without bacteria killing may be detrimental in some settings because live bacteria would be released, increasing the risk of recolonization and reinstatement of biofilms. These results demonstrate that catalytic NP-laden robots with designed geometries

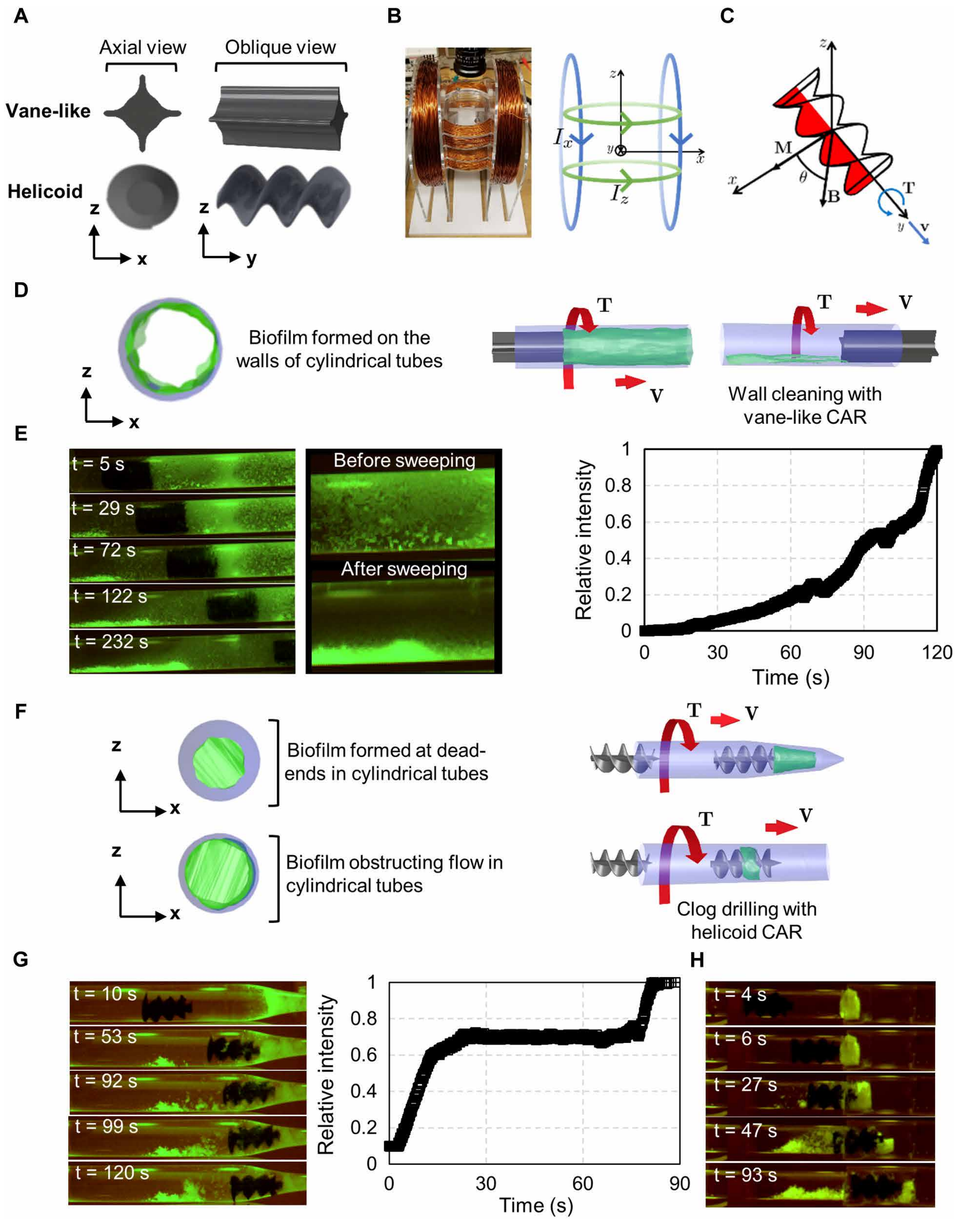

Fig. 5. Platform 2: Small-scale CARs with functional shapes for specific biofilm disruption tasks. (**A**) Model representations of vane-like and helicoid-shaped CARs fabricated from 3D micromolding agar gel embedded with NPs. Both vanes and helicoids measure 5 mm in diameter and 10 mm in length. The final robot composition is 3% (w/v) agar and 10% (w/v) NPs. (**B**) Helmholtz coil system used to drive 3D molded CARs through cylindrical tubes. Sinusoidal time-varying currents (I_x and I_z) were applied to each coil pair to generate uniform, rotating magnetic fields. Robots were driven using fields measuring 3.4 mT and rotating at 4 Hz. (**C**) Robots were driven through the cylindrical tube with linear velocity, v, which was generated by applying a torque, T, to the robot body. The torque was generated when the magnetic dipole moment, M, sought to align with the rotating field, B. (**D**) Schematic diagrams of biofilms on the wall of a cylindrical tube and wall cleaning by vane CAR. Vane CARs were used to clean the curved surfaces of glass tubes, rotated with an applied magnetic torque, T, and driven forward in the tube at a velocity, v, by applying a force using a magnetic field gradient. (**E**) Vane CARs advanced forward in the tube, sweeping the walls and generating a pile of debris behind them. The integrated fluorescence intensity from the biofilm debris increased with time behind the advancing robot. (Left) Accumulated biomass behind the vane CAR as it moved forward through the tube. (**F**) Schematic diagrams of biofilm clogs in cylindrical tubes and drilling by helicoid CARs. Helicoid CARs were used to clean biofilm clogs at various locations within the glass tube. The robots were propelled along linear paths within glass tubes through an applied magnetic torque, T. Their forward propulsion was enabled by their chirality. (**G**) A helicoid CAR advanced forward in the tube to drill through the biomass clog. (Left) Accumulated biomass behind the helicoid CAR as it moved forward through the tube increased with time. The robot drilled by overcoming the biofilm mechanical resistance associated with the conical shape of the biofilm (for $t < 30$ s for outer biomass removal and $t > 60$ s with additional force to penetrate the conical portion for the inner biomass removal) accumulated at the dead end of the confined space. (**H**) Helicoid CARs could also drill and restore biofilm-occluded paths. Fluorescent images showing the action and biofilm removal efficacy of vane-like (E) and helicoid (G and H) robots: green color indicates *S. mutans* biofilms or clogs.

can be propelled using magnetic torques to dismantle biofilms occluding tubes or on bounding surfaces and simultaneously to kill the dislodged bacterial cells.

We envision using CARs for effective treatment of biofilms on biotic and abiotic surfaces, a major unresolved problem that spans several scientific fields (dentistry, medicine, and engineering) and causes infectious diseases and biofouling in medical devices (Fig. 6A). To illustrate practical applications, we demonstrate the potential use of CARs to access the interior of human teeth (Materials and Methods). By using aggregated NPs, we applied the biohybrid CAR system to one of the most challenging anatomical areas of teeth, termed the isthmus; this is a narrow corridor (on order of hundreds of micrometers in width) between the root canals where bacterial biofilms often form. Currently available methods are unable to physically access or disinfect this anatomical region. In our demonstration, we first placed a droplet of the dispersed NPs suspension in the left side of the isthmus (Fig. 6B) and then we moved them using a permanent magnet coupled to a micromanipulator as described earlier (Fig. 4F). We observed aggregated NPs readily traversing the isthmus as directed by the external magnetic field (Fig. 6B). Then, we disrupted biofilms in the isthmus using fluorescently labeled biofilms by moving the biohybrid CARs in a back-and-forth motion (Fig. 6B, bottom middle panels). For 3D molded CARs, we actuated a miniaturized 3D molded CAR through the canal of the tooth, another common location of dental biofilm formation (Fig. 6C). Together, these examples illustrate feasibility and potential applications of controlled movement and specialized shapes to access, move, and target harmful biofilms.

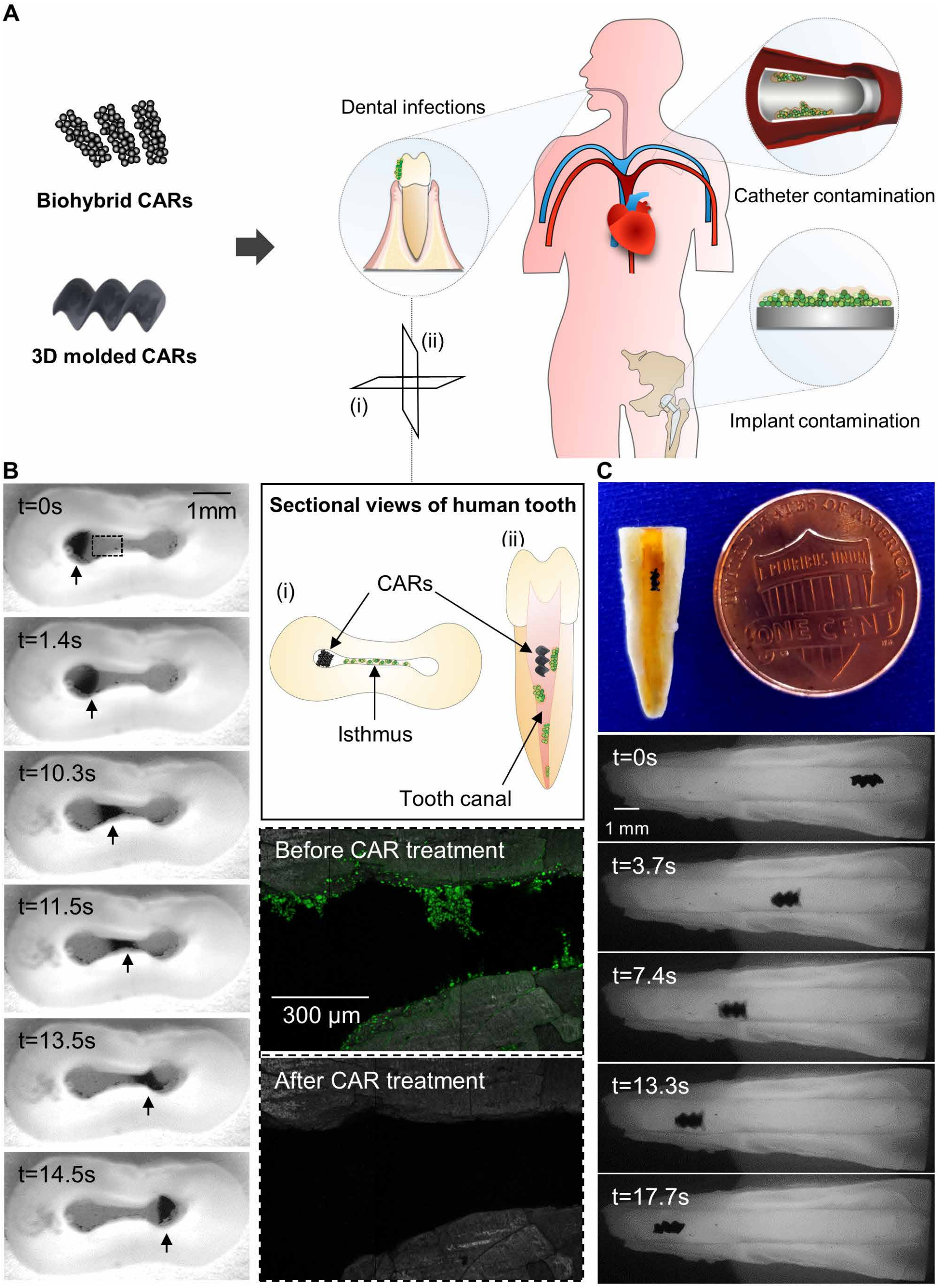

Fig. 6. Potential applications for CARs platforms. (**A**) CARs can be used to treat biofilms on biotic (e.g., teeth) and abiotic (catheter or implant) surfaces. (**B**) Demonstration of using CARs to access the interior of human teeth. Cross sections of the tooth canal show the isthmus, which is a narrow corridor (200 to 600 μm in width) between the root canals. A longitudinal section (across the tooth length) shows the tooth canal. Biohybrid CARs could access the isthmus, one of the most challenging anatomical areas of teeth, where bacterial biofilms are commonly found. Aggregated NPs could readily transverse the isthmus as directed by the external magnetic field. Lower middle panels show disruption of biofilms in the isthmus by CARS using fluorescently labeled biofilms. (**C**) For 3D molded CARs, miniaturized 3D molded helicoidal robots could be magnetically actuated through the canal of the tooth, another common location of dental biofilm formation.

DISCUSSION

In summary, we have introduced CARs as a modality for biofilm disruption and removal that can effectively address both biological and mechanical traits associated with biofilm recalcitrance and reinfection, a property unattainable using current approaches. By leveraging iron oxide NPs for their catalytic activity to kill and degrade the biofilm and driving CARs with external fields to physically disrupt the biomass and its debris, effective biofilm removal with high precision could be achieved using untethered, automated routines. In the first platform, biohybrid CARs were assembled from NPs and biofilm debris into superstructures that, when driven by an external magnetic field, plowed through and completely removed biofilms, preventing its regrowth altogether. This platform is suitable for biofilm removal from accessible and difficult-to-reach surfaces. In the second platform, 3D molded CARs with specialized shapes were designed to remove biofilms from confined spaces. Specifically, vane-shaped CARs removed biofilms from enclosed curved walls, and helicoid-shaped CARs drilled through biofilm clogs. Last, we demonstrated a practical application of CARs to target the interior of the human teeth, accessing and removing biofilms in a difficult-to-reach anatomical region termed isthmus. This robotic approach further advances previous iron oxide NP-based modalities that solely exploit magnetic properties (*6*, *7*, *31*). These modalities include magnetic actuation to induce hyperthermia for enhanced cell killing (*32*–*34*), to deliver antimicrobial drugs loaded into ferromagnetic NPs (*13*, *32*, *35*), or to cause topographical disturbances of ferrofluid-coated surfaces for disruption of algae accumulation (*14*). Complete biofilm elimination was achieved by exploiting simultaneously their catalytic and magnetic activation. Thus, we propose the synergistic kill-degrade-and-remove mechanism that underpins this antibiofilm performance. Such function provides a conceptual framework for a robotic platform that may be used across multiple disciplines to precisely and controllably eradicate harmful biological structures in medical and industrial settings, including catheters and water lines. Because the biohybrid CARs robots entrain the biomass, they can be also applied in diagnostics by retrieving microbial samples for compositional analyses. In addition, applications beyond biofilm disruption are possible because the inherent catalytic activity of iron oxide NPs has been used to detect/visualize (*36*, *37*) and to promote killing of cancer cells (*17*). Although this proof-of-concept work is still in an early phase, we envision a modular and scalable robotics platform using iron oxide NPs as building blocks to impart the catalytic and magnetic properties to the CARs. Additional mechanistic studies may elucidate the role of remanant magnetization and catalytic activity of different NP sizes for robotic assembly and biofilm removal on different surfaces and surface geometries. Further optimization and production may be feasible due to facile surface chemical modification and functionalization, as well as low-cost synthesis of these NPs at large scale (*36*), which could be adapted or complement bacterial targeting and toxin neutralization approaches, as reported recently (*38*). Magnetic nanomaterials with intrinsic catalytic “enzyme-mimetic” properties may have applications in other robotic systems that require biological functionalities and therapeutic properties.

MATERIALS AND METHODS

Synthesis of iron oxide NPs

Iron oxide NPs were synthesized in a solvothermal system and characterized as previously described (*10*). Briefly, 0.82 g of $FeCl_3$ was dissolved in 40 ml of ethylene glycol. Then, 3.6 g of sodium acetate was added to the solution with vigorous stirring for 30 min. The mixture was then transferred to a custom-built 50-ml Teflon-lined stainless steel autoclave and incubated at 200°C for 12 hours. After incubation, the iron oxide NP precipitate was collected, rinsed several times with ethanol, and then dried at 60°C for 3 hours. The synthesized NPs were characterized using scanning and transmission electron microscopy (JEOL 7500F and JEOL 2010F; JEOL USA, MA, USA). The peroxidase-like catalytic activity was tested via an established colorimetric assay using 3,3′,5,5′-tetramethylbenzidine as substrate, which generates a blue color with specific absorption at 652 nm as a result of reaction with free radicals generated by NPs in the presence of H_2O_2 (*10*).

Bacteria killing and EPS matrix degradation by NPs

Biofilms were formed on polystyrene dishes with inner circular glass bottom (MatTek dish; MatTek Corporation, Ashland, MA, USA). *Streptococcus mutans* UA159, a biofilm-forming model organism and a well-characterized oral pathogen, was grown in ultrafiltered (10-kDa cutoff; Millipore, MA, USA) tryptone-yeast extract (UFTYE) broth at 37°C and 5% CO_2 to mid-exponential phase (*39*). Each MatTek dish was inoculated with ~2×10^5 colony-forming units (CFU) of actively growing *S. mutans* cells per milliliter in UFTYE containing 1% (w/v) sucrose at 37°C with 5% CO_2 for 19 hours. Screening for optimal concentration of NPs and enzymes was performed to select the most effective bactericidal and EPS degradation activity (as detailed in the Supplementary Materials and fig. S1) for a formulation designed to enhance the catalytic bioactivity. The optimized concentrations of NPs (2000 $\mu g\ ml^{-1}$) with H_2O_2 (1%, v/v) and enzymes (dextranase/mutanase, 8.75/1.75 U ml^{-1}) were used for the biofilm disruption experiments. High-resolution confocal fluorescence imaging and standard culturing method (number of viable cells by CFU determination) were performed to assess the bacterial killing and EPS degradation of the formulation of NPs with H_2O_2/enzymes (*15*, *39*). NPs were topically applied onto the biofilm-covered surface, followed by addition of 1% H_2O_2 [in 0.1 M NaOAc buffer (pH 4.5)] and enzymes (dextranase/mutanase). For culturing method, the total number of CFU per biofilm was determined after biofilm treatment. Briefly, the treated biofilms were removed and homogenized via water bath sonication followed by probe sonication (30-s pulse at an output of 7 W; Branson Sonifier 150; Branson Ultrasonics, CT, USA). Homogenized biofilm suspensions were serially diluted and plated onto blood agar plates using an automated Eddy Jet Spiral Plater (Neutec Group Inc., Farmingdale, NY, USA), and the numbers of viable cells were determined by CFU counting. For fluorescence imaging, SYTO 9 (485/498 nm; Molecular Probes, Carlsbad, CA, USA) and propidium iodide (535/617 nm; Molecular Probes, Carlsbad, CA, USA) fluorescent probes were used for labeling live and dead bacteria, and Alexa Fluor 647 dextran conjugate (647/668 nm; Molecular Probes, Carlsbad, CA, USA) was used for labeling EPS (*39*). Confocal images were acquired in the same field of view at 0 and 60 min using a Zeiss LSM 800 upright laser scanning microscope (Carl Zeiss Microscopy GmbH, Jena, Germany) with a 20× (numerical aperture, 1.0) water immersion objective. Images were analyzed and processed using ImageJ and Amira 5.4.1 software (Visage Imaging, San Diego, CA, USA).

Modeling of magnetic flux density and actuation and characterization of NP aggregates

In experiments with NPs in suspension, NP aggregates were formed and actuated using a cylindrical permanent magnet through preprogrammed planar trajectories immediately below the surface. The permanent magnet was mounted to the arm of a Siskiyou four-axis nanomanipulator. The permanent magnet attached to the micromanipulator has a maximum magnetic flux density which measures 175 mT (MF100; Extech Instruments, Boston, MA, USA). To characterize the forces on the NP aggregate, we mathematically modeled magnetic flux density on a glass surface and observed NP aggregate motion within a model viscous fluid (glycerol). Using the maximum magnetic flux density of the permanent magnet along with its geometry, we developed a numerical simulation to compute the magnetic field using ANSYS software. In addition, we applied 100 μl of NP suspension [concentration ranging from 250 to 2000 $\mu g\ ml^{-1}$ in 50% (v/v) glycerol] over the glass surface and exposed it to a magnetic field generated by the permanent magnet for 300 s to characterize particle movement and size of the NP aggregate. Then, we moved the NP aggregate along preprogrammed trajectories coded in Python using custom libraries to confirm the proper actuation of the NPs. Videos of the NP aggregate assembly and movement dynamics were captured using a Point Grey Flea3 Monochrome camera outfitted with a 6-mm Navitar lens at a video frame of 10 fps. Still images were also extracted and processed with Otsu's thresholding method using ImageJ. Then, changes in particle density and size of the clusters were quantified using MATLAB image-processing libraries and ImageJ. We measured the rate of movement of a cluster of NPs in 50% glycerol (density, 1126.3 kg m^{-3}; dynamic viscosity, 5 mPa s^{-1}) to approximate the maximum Reynolds number. The speed of a 2-μm cluster was 1.6 μm s^{-1} in the region of highest field gradient. The Reynolds number was on the order of 10^{-7}, well within the low Reynolds number regime. Thus, inertia was negligible and Stokes law was applicable. Given this velocity, particle size, and drag coefficient, the viscous drag force on a representative 2-μm NP aggregate was estimated, from Stokes law, to be ~30 pN. Because other forces were negligible, we estimated the magnetic force to be equivalent in magnitude to the drag force with opposite direction.

Furthermore, we also characterized the behavior of NP suspension and aggregate formation on the *S. mutans* biofilm. Biofilms were formed on the planar surface of a MatTek dish for 19 hours as described in the previous section and then treated with NP suspension. Biofilm cells were labeled with SYTO 82 (541/560 nm; Molecular Probes, Carlsbad, CA, USA), and the NPs were detected via inherent reflectance optical property using confocal microscopy. To investigate NP motion and aggregation dynamics, we conducted experiments with either NP with catalysis or NP alone (without catalysis). One hundred microliters of enzyme solution [dextranase/mutanase, 8.75/1.75 U in 0.1 M NaOAc buffer (pH 4.5)] was applied on the biofilm surface, followed by 100 μl of NP suspension [2000 μg ml^{-1} in 0.1 M NaOAc buffer (pH 4.5)] with 1% H_2O_2 and incubated at room temperature for 30 min. In NP alone, the same procedure was conducted using the same amount of NPs in NaOAc buffer without enzymes and H_2O_2. After incubation, biofilms were exposed to a magnetic field generated by the permanent magnet for 120 s. Videos of the NP aggregate movement process on biofilms were captured using a Zeiss AxioVision fluorescence upright microscope system (Carl Zeiss Microscopy GmbH, Jena, Germany) or a Wild stereoscope (Wild Heerbrugg, Switzerland). Still images were processed and quantified using ImageJ. We also examined the detailed structural organization of the NPs in treated biofilms using a Zeiss LSM 800 microscope with a 20× (numerical aperture, 1.0) water immersion objective. NPs were detected via a 405-nm laser with a 445/50 nm emission filter, and biofilm cells were detected by a 560-nm laser with a 590/60 emission filter. Images were processed and reconstructed by Amira and ImageJ. In addition, the bactericidal and EPS degrading activity of NP with catalysis or NP alone (without catalysis) was determined by culturing and fluorescence methods as described in the previous section. Biofilm analyses revealed that NP with catalysis killed bacteria and disrupted EPS and the magnetic field assembled NPs and the biodegraded products into rod-like structures, which moved in a controlled manner to generate a biohybrid CAR.

Biofilm removal by biohybrid CARs

Biofilms were formed on the planar surface of a MatTek dish as described above and treated with catalytic NPs formulation. For large-scale (broad swathes) biofilm removal, 200 μg of NPs in 100 μl of 0.1 M NaOAc buffer solution (pH 4.5) with optimized H_2O_2/enzymes were sequentially applied onto the biofilm surface. For precision cleaning, a small volume of concentrated NP suspension (100 μg in 20 μl) was applied in a specific location of the biofilm surface, followed by adding 80 μl of buffer solution without disturbing the localized NP spot. After a 30-min incubation, the NPs were exposed to magnetic field, and biohybrid CARs were locally assembled and driven along preprogrammed trajectories, forming a biofilm-removing plow. Actuation in all experiments was performed via application of an external magnetic field programmed to achieve a desired motion pattern. Sensing was achieved via a charge-coupled device camera, which can be used for visual feedback in a closed-loop system (*40*). The control algorithms for this work were programmed using open-loop control, in which motion patterns were preprogrammed on the basis of modeling of system dynamics. The open-loop driving and control algorithms were chosen because they were simple and flexible, enabling a variety of locomotion with high precision. Videos of the removal process were captured using a Point Grey Flea3 Monochrome camera outfitted with a 6-mm Navitar lens at a video frame rate of 10 fps. After biofilm removal, the cleared area was imaged to confirm bacterial killing and complete removal of biomass from the surface using confocal fluorescence microscopy and culturing methods as detailed earlier. In addition, we investigated whether biofilm could regrow from the cleared area. After biofilm killing and removal by CAR treatment, we incubated the cleared area in UFTYE broth at 37°C and 5% CO_2 for an additional 24 hours. Biofilms treated with buffer or NP alone (without catalysis) were also incubated for 24 hours to demonstrate bacterial viability and further biofilm growth in the absence of CARs. After incubation, biofilms were collected for confocal fluorescence imaging, quantification of the number of viable cells (CFU counting), and determination of total biomass (dry weight).

Design of small-scale 3D molded CARs

Robots were designed and fabricated using a 3D micromolding technique resembling injection molding method (*20*, *41*). This process enabled direct fabrication of custom, shape-specific millimeter-scale robots that were composed of agar gel (Difco, BD Biosciences, Sparks, MD, USA) embedded with NPs. Briefly, two-piece negative molds were designed in SolidWorks and 3D printed using a Projet 6000 HD stereolithography printer. Two different robot shapes (helicoids and vanes) were designed for operation in cylindrical tubes. Agar gel was heated above 80°C, vigorously mixed with NPs, and poured into the mold. The resulting robot profiles solidified at room temperature. The final robot composition was 3% (w/v) agar and 10% (w/v) NPs. The smallest robots used in the tooth included 25% glycerol to reduce drying and warping before mold extraction. Robots were manually removed from the molds and premagnetized along their short axis with a neodymium iron boron (NdFeB) magnet. For the results presented in this work, CAR sizes were selected for given application spaces, including biofilm-coated tubes (7-mm diameter) or internal architecture of the tooth (canal: 1.5- to 1.8-mm diameter).

Actuation and control of small-scale 3D molded CARs

Small-scale CARs produced via micromolding were driven using uniform, rotating magnetic fields that were generated using two pairs of nested Helmholtz coils as previously described (*20*). Each coil pair was driven independently using a programmable power supply and a custom program written in C++. The magnetic field strength and rotational frequency were controlled independently. The robots were magnetized perpendicular to their long axis or direction of travel. Rotating magnetic fields were applied to realign the robots. In all experiments, magnetic fields rotating at 2 or 4 Hz were applied, and robots were operated at the center of the workspace where fields were approximately uniform and measure 3.4 mT (MF100; Extech Instruments, Boston, MA, USA). In addition, a magnetic field gradient was applied using a permanent magnet to drive forward the vane CARs or to provide additional strength for the helicoid CARs to drill through the biomass clog. Robots executed preprogrammed trajectories within a glass tube measuring 600 mm long and 7 mm in diameter. Experiments were recorded at 10 fps using a Point Grey Flea3 Monochrome camera mounted adjacent to the outer coils such that the entire length of the tube is in the field of view. To determine the robot's position and velocity, videos were processed using standard OpenCV libraries.

Biofilm removal by small-scale 3D molded CARs

Pasteur Pipets (Pyrex Borosilicate Glass; VWR International, PA, USA) were cut to specific dimensions: (i) 450-mm length and 7-mm diameter with open end (type I) and (ii) 550-mm length with closed conical end (type II). Then, each customized Pasteur Pipet was sterilized by autoclaving and inoculated with about 2×10^5 CFU of *S. mutans* per ml in UFTYE containing 1% (w/v) sucrose at 37°C with 5% CO_2. To form a biofilm that coated the walls of the tube, we added 2 ml of the inoculated culture medium to type I tube. Biofilms were cultured for 42 hours, and the culture medium was changed at 19 and 29 hours. Alternatively, 200 μl of the inoculated culture medium was added to a type II tube to form biofilm clogs at the end of the conical portion of the tube. In addition, biofilms were also prepared to mimic clogs in the center of the tube. To achieve this, we harvested preformed biofilms that were cultured for 42 hours on MatTek dishes and transferred them to the open end of the type I tube using a spatula to create a biofilm clog. Then, the occluded end of the tube was connected with transparent Tygon tubing (inside diameter, 6.4 mm; outside diameter, 9.5 mm) (AAA00017; Cole-Parmer, Chicago, IL, USA). The biofilm was labeled with green fluorescent protein (SYTO 9) for visualization and quantification purposes. Helicoid and vane robots were driven along preprogrammed trajectories to clear biofilms from the inner tube wall surface and to ablate biofilm clogs. Videos of the removal process were captured using a frame rate of 10 fps (Point Grey Flea3 Monochrome, 6-mm Navitar lens). Illumination of the experimental workspace was done with blue excitation LEDs (470 nm) along with an amber acrylic emission filter (McMaster-Carr), which enabled a fluorescence imaging of biofilms. Image frames were processed to determine the amount of biomass removed by the robot. Biofilm relative accumulation was determined by integrating the green channel value in the pixels of an increasingly rectangular area formed as the robot advanced through the tubing. This was done using custom libraries for image analysis in Python (skimage, PIL).

Application of CARs in human tooth model

To illustrate practical application of CARs, we demonstrate the potential use of CARs to access the interior of human tooth using discarded extracted teeth. Two different preparations were used: (i) cross section for isthmus and (ii) longitudinal section for root canal. To prepare the specimens, we removed the crowns of single-root teeth at the cemento-enamel junction using a 0.6-mm-thick precision diamond saw (Isomet 5000; Buehler Ltd., Lake Bluff, IL) at 1000 rpm under water cooling. Canals were enlarged using XP-endo 3D Shaper (Brasseler USA, Savannah, GA) at 1000 rpm followed by Endosequence files, size nos. 40, 50, and 60 (Brasseler USA, Savannah, GA). We then prepared root vertical sections by vertically sectioning the root segments using a 0.6-mm-thick precision diamond saw (Isomet 5000; Buehler Ltd., Lake Bluff, IL) at 1000 rpm under water cooling. The canal space was then enlarged with Gates Glidden drill no. 6 (Tulsa Dentsply, Tulsa, OK) at 300 rpm under water cooling to produce a canal space diameter of ~1.5 mm. Horizontal isthmus sections were prepared by sectioning the coronal segment of the mesial root of the first molar using a 0.6-mm-thick precision diamond saw; after visual confirmation of the presence of the isthmus, we enlarged the canals on the horizontal sections using Gates Glidden drill no. 6 (to reach 300 to 500 μm in diameter) at 300 rpm under water cooling. Vertical and horizontal sections were then treated with 6% NaOCl followed by 17% ethylenediaminetetraacetic acid solution (Vista Dental Products, Racine, WI, USA) in an ultrasonic bath for 10 min each, followed by a 10-min bath sonication in sterile water to remove the residual effect of the chemicals. Specimens were then sterilized in an autoclave for 20 min at 121°C. To demonstrate movement of the CARs inside the isthmus specimen, we placed the specimen in 2 ml of water in a MatTek dish, and 1 μl of NP suspension [5000 $\mu g\ ml^{-1}$ in 0.1 M NaOAc buffer (pH 4.5)] was topically placed at one canal end in the isthmus. Then, the sample was exposed to a magnetic field generated by the permanent magnet mounted on a four-axis nanomanipulator as described in the previous section. Then, videos of the NP movement in isthmus were captured using a Zeiss Axio Zoom.V16 fluorescence upright stereo zoom microscope system (Carl Zeiss Microscopy GmbH, Jena, Germany) with a 1× objective (numerical aperture, 0.25). To demonstrate biofilms disruption, we inoculated isthmus samples with ~2×10^5 CFU of *S. mutans* or *Enterococcus faecalis* per ml in a 24-well culture plate containing low molecular weight medium and 1% (w/v) sucrose at 37°C with 5% CO_2 for 18 hours. The specimens were then washed in 0.89% NaCl sterile saline solution using dip washing method to remove unattached cells. The samples were treated and exposed to a magnetic field as described in the previous section. We examined biofilm removal on the isthmus before and after CAR actuation using a Zeiss LSM 800 microscope with a 10× (numerical aperture, 0.4) air objective. Tooth was detected via a 405-nm laser with a 445/50 nm emission filter, and biofilm cells were detected by a 488-nm laser with a 500/40 emission filter. Images were processed and reconstructed by ImageJ. To demonstrate movement of the CARs inside the vertical canal sample, we prepared miniaturized 3D molded helicoid CARs using 1-mm molds. Because it was a water-based hydrogel, it dehydrated in ambient conditions before experiments, resulting in a slightly smaller size of ~700 μm by 1.5 mm, which is consistent with our previous methods (*20*, *41*). The specimen was placed horizontally in 3 ml of water in a MatTek dish, the robot was placed inside the canal, and a cover glass was placed on top of the specimen to create a seal. The robot was driven using uniform, rotating magnetic fields that were generated using two pairs of nested Helmholtz coils as described in the previous section.

Statistical analyses

The data were analyzed by pairwise comparisons of multiple groups with regression models using ranked values. Kruskal-Wallis test (nonparametric and based on ranks) was used for two-group comparisons. The significance levels were set at 5%, and no adjustments were made for multiple comparisons. SAS statistical software, version 9.3 (SAS Institute, Cary, NC) was used to perform the analyses.

SUPPLEMENTARY MATERIALS

robotics.sciencemag.org/cgi/content/full/4/29/eaaw2388/DC1
Materials and Methods
Discussion
Fig. S1. Optimization of concentrations of NPs and enzymes and application/biological functions of NPs with catalysis.
Fig. S2. Characterization of NPs in model solution.
Fig. S3. Biohybrid CAR formed from bio-inorganic superstructure.
Fig. S4. Biohybrid CAR assembly and biofilm removal.
Fig. S5. Viability of bacterial cells in biofilms after CAR treatment.
Fig. S6. Biofilm removal using biohybrid Feraheme (ferumoxytol) CARs.
Fig. S7. Catalytic activity of 3D molded CARs.
Fig. S8. Vane-like CARs for cleaning the curved surfaces of glass tubes.
Fig. S9. Characterization of response of helicoid robot to various conditions.
Fig. S10. Assessment of biofilm removal using 3D molded CARs with and without catalytic activity.
Movie S1. Application of controlled movement of focused CARs for precision removal of biofilms from surface (Fig. 4F).
Movie S2. Application of helicoid CARs for removal of biofilms from the curved surfaces of glass tubes (Fig. 5G).

REFERENCES AND NOTES

1. D. Lebeaux, J.-M. Ghigo, C. Beloin, Biofilm-related infections: Bridging the gap between clinical management and fundamental aspects of recalcitrance toward antibiotics. *Microbiol. Mol. Biol. Rev.* **78**, 510–543 (2014).
2. H.-C. Flemming, J. Wingender, U. Szewzyk, P. Steinberg, S. A. Rice, S. Kjelleberg, Biofilms: An emergent form of bacterial life. *Nat. Rev. Microbiol.* **14**, 563–575 (2016).
3. H. Koo, R. N. Allan, R. P. Howlin, P. Stoodley, L. Hall-Stoodley, Targeting microbial biofilms: Current and prospective therapeutic strategies. *Nat. Rev. Microbiol.* **15**, 740–755 (2017).
4. B. W. Peterson, Y. He, Y. Ren, A. Zerdoum, M. R. Libera, P. K. Sharma, A. J. van Winkelhoff, D. Neut, P. Stoodley, H. C. van der Mei, H. J. Busscher, Viscoelasticity of biofilms and their recalcitrance to mechanical and chemical challenges. *FEMS Microbiol. Rev.* **39**, 234–245 (2015).
5. J. Li, B. E.-F. de Ávila, W. Gao, L. Zhang, J. Wang, Micro/nanorobots for biomedicine: Delivery, surgery, sensing, and detoxification. *Sci. Robot.* **2**, eaam6431 (2017).
6. M. Sitti, Miniature soft robots—Road to the clinic. *Nat. Rev. Mater.* **3**, 74–75 (2018).
7. B. J. Nelson, I. K. Kaliakatsos, J. J. Abbott, Microrobots for minimally invasive medicine. *Annu. Rev. Biomed. Eng.* **12**, 55–85 (2010).
8. X.-Z. Chen, M. Hoop, F. Mushtaq, E. Siringil, C. Hu, B. J. Nelson, S. Pané, Recent developments in magnetically driven micro- and nanorobots. *Appl. Mater. Today* **9**, 37–48 (2017).
9. X. Ma, S. Sánchez, Self-propelling micro-nanorobots: Challenges and future perspectives in nanomedicine. *Nanomedicine* **12**, 12 (2017).
10. L. Gao, J. Zhuang, L. Nie, J. Zhang, Y. Zhang, N. Gu, T. Wang, J. Feng, D. Yang, S. Perrett, X. Yan, Intrinsic peroxidase-like activity of ferromagnetic nanoparticles. *Nat. Nanotechnol.* **2**, 577–583 (2007).
11. L. Gao, K. M. Giglio, J. L. Nelson, H. Sondermann, A. J. Travis, Ferromagnetic nanoparticles with peroxidase-like activity enhance the cleavage of biological macromolecules for biofilm elimination. *Nanoscale* **6**, 2588–2593 (2014).
12. L. Gao, Y. Liu, D. Kim, Y. Li, G. Hwang, P. C. Naha, D. P. Cormode, H. Koo, Nanocatalysts promote *Streptococcus mutans* biofilm matrix degradation and enhance bacterial killing to suppress dental caries in vivo. *Biomaterials* **101**, 272–284 (2016).
13. B. M. Geilich, I. Gelfat, S. Sridhar, A. L. van de Ven, T. J. Webster, Superparamagnetic iron oxide-encapsulating polymersome nanocarriers for biofilm eradication. *Biomaterials* **119**, 78–85 (2017).
14. W. Wang, J. V. I. Timonen, A. Carlson, D.-M. Drotlef, C. T. Zhang, S. Kolle, A. Grinthal, T.-S. Wong, B. Hatton, S. H. Kang, S. Kennedy, J. Chi, R. T. Blough, M. Sitti, L. Mahadevan, J. Aizenberg, Multifunctional ferrofluid-infused surfaces with reconfigurable multiscale topography. *Nature* **559**, 77–82 (2018).
15. Y. Liu, P. C. Naha, G. Hwang, D. Kim, Y. Huang, A. Simon-Soro, H.-I. Jung, Z. Ren, Y. Li, S. Gubara, F. Alawi, D. Zero, A. T. Hara, D. P. Cormode, H. Koo, Topical ferumoxytol nanoparticles disrupt biofilms and prevent tooth decay in vivo via intrinsic catalytic activity. *Nat. Commun.* **9**, 2920 (2018).
16. M. F. Hayacibara, H. Koo, A. M. Vacca Smith, L. K. Kopec, K. Scott-Anne, J. A. Cury, W. H. Bowen, The influence of mutanase and dextranase on the production and structure of glucans synthesized by streptococcal glucosyltransferases. *Carbohydr. Res.* **339**, 2127–2137 (2004).
17. S. Zanganeh, G. Hutter, R. Spitler, O. Lenkov, M. Mahmoudi, A. Shaw, J. S. Pajarinen, H. Nejadnik, S. Goodman, M. Moseley, L. M. Coussens, H. E. Daldrup-Link, Iron oxide nanoparticles inhibit tumour growth by inducing pro-inflammatory macrophage polarization in tumour tissues. *Nat. Nanotechnol.* **11**, 986–994 (2016).
18. J. Paik, Soft robot design methodology for 'push-button' manufacturing. *Nat. Rev. Mater.* **3**, 81–83 (2018).
19. S. V. Murphy, A. Atala, 3D bioprinting of tissues and organs. *Nat. Biotechnol.* **32**, 773–785 (2014).
20. E. E. Hunter, E. W. Brink, E. B. Steager, V. Kumar, Toward soft micro bio robots for cellular and chemical delivery. *IEEE Robot. Autom. Lett.* **3**, 1592–1599 (2018).
21. M. S. Sakar, E. B. Steager, D. H. Kim, M. J. Kim, G. J. Pappas, V. Kumar, Single cell manipulation using ferromagnetic composite microtransporters. *Appl. Phys. Lett.* **96**, 043705 (2010).
22. C. Peters, O. Ergeneman, P. D. W. García, M. Müller, S. Pané, B. J. Nelson, C. Hierold, Superparamagnetic twist-type actuators with shape-independent magnetic properties and surface functionalization for advanced biomedical applications. *Adv. Funct. Mater.* **24**, 5269–5276 (2014).
23. G. Hwang, M. I. Klein, H. Koo, Analysis of the mechanical stability and surface detachment of mature *Streptococcus mutans* biofilms by applying a range of external shear forces. *Biofouling* **30**, 1079–1091 (2014).
24. X.-Z. Chen, B. Jang, D. Ahmed, C. Hu, C. De Marco, M. Hoop, F. Mushtaq, B. J. Nelson, S. Pané, Small-scale machines driven by external power sources. *Adv. Mater.* **30**, 1705061 (2018).
25. T. Honda, K. I. Arai, K. Ishiyama, Micro swimming mechanisms propelled by external magnetic fields. *IEEE Trans. Magn.* **32**, 5085–5087 (1996).
26. J. J. Abbott, K. E. Peyer, L. X. Dong, B. J. Nelson, How Should Microrobots Swim? in *Robotics Research* (Springer, 2010), pp. 157–167.
27. K. Ishiyama, M. Sendoh, A. Yamazaki, K. I. Arai, Swimming micro-machine driven by magnetic torque. *Sens. Actuators A Phys.* **91**, 141–144 (2001).
28. I. S. Khalil, A. F. Tabak, K. Sadek, D. Mahdy, N. Hamdi, M. Sitti, Rubbing against blood clots using helical robots: Modeling and in vitro experimental validation. *IEEE Robot. Autom. Lett.* **2**, 927–934 (2017).
29. G. Hwang, B. Koltisko, X. Jin, H. Koo, Nonleachable imidazolium-incorporated composite for disruption of bacterial clustering, exopolysaccharide-matrix assembly, and enhanced biofilm removal. *ACS Appl. Mater. Interfaces* **9**, 38270–38280 (2017).
30. J. J. Abbott, K. E. Peyer, M. C. Lagomarsino, L. Zhang, L. Dong, I. K. Kaliakatsos, B. J. Nelson, How should microrobots swim? *Int. J. Robot. Res.* **28**, 1434–1447 (2009).
31. N. Lee, D. Yoo, D. Ling, M. H. Cho, T. Hyeon, J. Cheon, Iron oxide based nanoparticles for multimodal imaging and magnetoresponsive therapy. *Chem. Rev.* **115**, 10637–10689 (2015).
32. S. Carregal-Romero, P. Guardia, X. Yu, R. Hartmann, T. Pellegrino, W. J. Parak, Magnetically triggered release of molecular cargo from iron oxide nanoparticle loaded microcapsules. *Nanoscale* **7**, 570–576 (2015).
33. M. Azhdarzadeh, F. Atyabi, A. A. Saei, B. S. Varnamkhasti, Y. Omidi, M. Fateh, M. Ghavami, S. Shanehsazzadeh, R. Dinarvand, Theranostic MUC-1 aptamer targeted gold coated superparamagnetic iron oxide nanoparticles for magnetic resonance imaging and photothermal therapy of colon cancer. *Colloids Surf. B Biointerfaces* **143**, 224–232 (2016).
34. Z. Wang, R. Qiao, N. Tang, Z. Lu, H. Wang, Z. Zhang, X. Xue, Z. Huang, S. Zhang, G. Zhang, Y. Li, Active targeting theranostic iron oxide nanoparticles for MRI and magnetic resonance-guided focused ultrasound ablation of lung cancer. *Biomaterials* **127**, 25–35 (2017).
35. T. Todd, Z. Zhen, W. Tang, H. Chen, G. Wang, Y.-J. Chuang, K. Deaton, Z. Pan, J. Xie, Iron oxide nanoparticle encapsulated diatoms for magnetic delivery of small molecules to tumors. *Nanoscale* **6**, 2073–2076 (2014).
36. D. P. Cormode, L. Gao, H. Koo, Emerging biomedical applications of enzyme-like catalytic nanomaterials. *Trends Biotechnol.* **36**, 15–29 (2017).
37. K. Fan, C. Cao, Y. Pan, D. Lu, D. Yang, J. Feng, L. Song, M. Liang, X. Yan, Magnetoferritin nanoparticles for targeting and visualizing tumour tissues. *Nat. Nanotechnol.* **7**, 459–464 (2012).
38. B. E.-F. de Ávila, P. Angsantikul, D. E. Ramírez-Herrera, F. Soto, H. Teymourian, D. Dehaini, Y. Chen, L. Zhang, J. Wang, Hybrid biomembrane–functionalized nanorobots for concurrent removal of pathogenic bacteria and toxins. *Sci. Robot.* **3**, eaat0485 (2018).
39. J. Xiao, M. I. Klein, M. L. Falsetta, B. Lu, C. M. Delahunty, J. R. Yates III, A. Heydorn, H. Koo, The exopolysaccharide matrix modulates the interaction between 3D architecture and virulence of a mixed-species oral biofilm. *PLOS Pathog.* **8**, e1002623 (2012).
40. E. B. Steager, M. Selman Sakar, C. Magee, M. Kennedy, A. Cowley, V. Kumar, Automated biomanipulation of single cells using magnetic microrobots. *Int. J. Robot. Res.* **32**, 346–359 (2013).
41. E. E. Hunter, E. W. Brink, E. B. Steager, V. Kumar, 3D Micromolding of small-scale biological robots, in *2018 International Conference on Manipulation, Automation and Robotics at Small Scales (MARSS)* (IEEE, 2018).

Funding: This work was supported, in part, by the National Institute for Dental and Craniofacial Research, National Institutes of Health (R01DE025848 and R01DE018023), and the National Science Foundation (NSF 1446592). Y.L. is the recipient of Colgate-Palmolive Fellowship in Pediatric Dentistry for the Doctor of Science in Dentistry (DScD) program at Penn Dental Medicine, E.E.H. is the recipient of National Science Foundation Graduate Research Fellowship grant (DGE-1845298), and A.J.P. is the recipient of the Brazilian agency CAPES scholarship grant (88881.119452/2016-01). The authors are also thankful for support from the University Research Foundation, University of Pennsylvania. **Author contributions:** G.H., A.J.P., E.S., and H.K. conceived the work. G.H., A.J.P., E.E.H., E.S., and H.K. designed the experiments and analyzed the data. G.H., A.J.P., E.E.H., Y.L., A.B., B.K., and E.S. performed the experiments. G.H., A.J.P., E.E.H., K.S., E.S., and H.K. wrote the manuscript. G.H., A.J.P., E.E.H., K.S., V.K., E.S., A.B., B.K., and H.K. assisted in writing and editing the manuscript. **Competing interests:** H.K., K.S., V.K., E.E.H., and E.S. are inventors on a patent application (62/772,306) submitted by the University of Pennsylvania that covers small-scale robots for biofilm eradication. The other authors declare that they have no competing financial interests. **Data and materials availability:** All data needed to evaluate the conclusions in the paper are present in the paper or the Supplementary Materials.

Submitted 3 December 2018
Accepted 29 March 2019
Published 24 April 2019
10.1126/scirobotics.aaw2388

Citation: G. Hwang, A. J. Paula, E. E. Hunter, Y. Liu, A. Babeer, B. Karabucak, K. Stebe, V. Kumar, E. Steager, H. Koo, Catalytic antimicrobial robots for biofilm eradication. *Sci. Robot.* **4**, eaaw2388 (2019).

Science Robotics

Catalytic antimicrobial robots for biofilm eradication

Geelsu Hwang, Amauri J. Paula, Elizabeth E. Hunter, Yuan Liu, Alaa Babeer, Bekir Karabucak, Kathleen Stebe, Vijay Kumar, Edward Steager, and Hyun Koo

Sci. Robot. **4** (29), eaaw2388. DOI: 10.1126/scirobotics.aaw2388

Science Robotics (ISSN 2470-9476) is published by the American Association for the Advancement of Science. 1200 New York Avenue NW, Washington, DC 20005. The title *Science Robotics* is a registered trademark of AAAS.